PCCP

ROYAL SOCIETY OF CHEMISTRY

PAPER

View Article Online
View Journal | View Issue

Cite this: *Phys. Chem. Chem. Phys.*, 2023, **25**, 15885

Rocking motion in solid proteins studied by the ^{15}N proton-decoupled $R_{1\rho}$ relaxometry†

Alexey Krushelnitsky,* Günter Hempel, Hannes Jurack and Tiago Mendes Ferreira

Recently it has been revealed that proteins in solid samples undergo slow overall rocking. The parameters of this motion depend on intermolecular interactions. Therefore, the characterization of the rocking motion enables one to investigate protein–protein interactions. NMR $R_{1\rho}$ relaxometry is the most suitable tool to study slow molecular motions. However, the time scale of the rocking motion is on the edge of the dynamics window of the standard $R_{1\rho}$ experiment, precluding the $R_{1\rho}$ data analysis from being precise and reliable. In this work, we apply a modified $R_{1\rho}$ relaxation method to characterize the slow motion in solids with much higher precision and reliability. The modification is the simultaneous use of a strong ^{1}H-CW pulse and a weak/moderate ^{15}N spin-lock pulse. We demonstrate theoretically and experimentally that under this condition, $R_{1\rho}$ decays have a significantly better signal-to-noise ratio and a much shorter "dead time" caused by the initial oscillations compared to the conventional $R_{1\rho}$ experiment. Moreover, the proton-decoupled $R_{1\rho}$'s can be measured at a much smaller difference between the spin-lock and MAS frequencies; thus, much slower molecular motions can be sampled. The proton decoupling during the ^{15}N spin-lock pulse also suppresses the interfering coherent spin–spin relaxation pathway at low spin-lock fields, which overlaps the Bloch–McConnell (chemical exchange) range of $R_{1\rho}$ dispersions. The proton-decoupled and standard $R_{1\rho}$ experiments were used to study the rocking motion of ^{15}N,^{2}H-enriched protein GB1 in two solid forms, microcrystals and lyophilized amorphous powder. The most striking finding is that the correlation function of this motion consists of two components with very different correlation times, 2–20 μs and a few hundred μs. The rocking motion parameters in microcrystals and powder are quite different, revealing the distinct nature of inter-protein interactions in these two samples.

Received 27th January 2023,
Accepted 12th May 2023

DOI: 10.1039/d3cp00444a

rsc.li/pccp

Introduction

$R_{1\rho}$-relaxometry is a powerful NMR technique that enables a detailed study of molecular dynamics in the microsecond time scale.[1–7] Unlike measurements of the motionally averaged dipolar, quadrupolar or chemical shift anisotropy (CSA) interactions, the relaxation methods allow obtaining both amplitudes and correlation times of molecular motions. This is why the relaxation experiments are more informative, although more time-consuming than many other experimental approaches. The relaxation rate is proportional to the spectral density function $J(\omega)$, where $\omega/2\pi$ is the resonance (for the case of R_1) or spin-lock (for the case of $R_{1\rho}$) frequency. To get more exact information on the correlation function of motion, one has to measure the relaxation rates in a wide range of ω. There are, however, some natural limitations in varying ω that are difficult to circumvent. Large ω values in $R_{1\rho}$-experiments are limited by the hardware (amplifiers and probes) and the sample heating effect. On the other hand, the spin-lock field in static experiments cannot be set to values lower or comparable to the local field since the relaxation, in this case, is dependent on both spin-lock and local fields, and the data analysis would be more difficult and ambiguous. Under magic angle spinning (MAS), the $R_{1\rho}$ relaxation rate corresponding to the heteronuclear dipolar and CSA relaxation mechanisms is proportional to the combination of the spectral density functions $J(\omega_{SL} \pm \omega_{MAS})$ and $J(\omega_{SL} \pm 2\omega_{MAS})$,[2,8,9] where $\omega_{SL}/2\pi$ and $\omega_{MAS}/2\pi$ are the spin-lock and MAS frequencies. Setting $\omega_{SL} = \omega_{MAS}$ or $\omega_{SL} = 2\omega_{MAS}$ (rotary resonance conditions, at which the anisotropic interactions are recoupled) unfortunately does not allow measuring $J(0)$, that is the low-frequency limit of the spectral density function. In this case, the amplitude of the relaxation decay becomes zero, and the

Institut für Physik, Martin-Luther-Universität Halle-Wittenberg, Betty-Heimann-Str. 7, 06120, Halle (Saale), Germany. E-mail: krushelnitsky@physik.uni-halle.de

† Electronic supplementary information (ESI) available: Details of the relaxation decays analysis; results of the data fitting assuming distribution of the correlation times; details of measurements ^{1}H-^{15}N dipolar couplings; details of quantifying the rf-pulses heating effect; analytical derivation of eqn (3); Spinach code for the $R_{1\rho}$ numerical simulations. See DOI: https://doi.org/10.1039/d3cp00444a

amplitude of the initial transient oscillations of the decay (see detailed discussion below) becomes so large that the reliable determination of the relaxation rate in the vicinity of the rotary resonance condition is simply impossible.[10]

In this work, we apply a modification of the $R_{1\rho}$ experiment to suppress these interfering effects and to observe slower motions that are not possible to observe using only a standard conventional $R_{1\rho}$ pulse sequence. This modification is a high-power proton decoupling during the X-channel spin-lock pulse (Fig. 1). This approach was first suggested about 20 years ago.[11] Effectively, the proton decoupling can "switch off" the dipolar relaxation mechanism of slow molecular motions and thus, the $R_{1\rho}$ relaxation is caused dominantly by the CSA mechanism. The proton decoupling also suppresses the interfering coherent spin–spin relaxation mechanism,[12] and thus, the relaxation rates can be measured and rigorously analysed at small spin-lock fields, which is impossible using a standard $R_{1\rho}$ experiment. This method was applied in some previous studies of biomolecular dynamics,[13,14] however, this was done only in a phenomenological fashion.

Here we present an analytical and numerical description of this experiment and demonstrate its advantages by applying it to studying a specific type of molecular mobility – rocking motions of proteins in solid samples. Proteins in solid state (*e.g.* in microcrystals) are not rigidly fixed by inter-molecular contacts; they undergo restricted motion as a whole. This kind of protein dynamics was reported for the first time by Paul Schanda and co-workers,[15] and then this observation was confirmed in a few subsequent studies.[10,16,17] Using standard ^{15}N $R_{1\rho}$ experiments, the angular amplitude and the time scale of the rocking motion were estimated to be only few degrees and few tens microseconds, respectively.[10] These numbers are however not precise since this motional time scale is on the edge of the dynamic window of the standard $R_{1\rho}$ experiment. As shown below, the proton-decoupled ^{15}N $R_{1\rho}$ experiment enables to extend this window towards slower motions. This approach is demonstrated in the comparative experimental study of the same protein (GB1) in two different solid forms – microcrystals and lyophilized amorphous powder. The parameters of the rocking motion are obviously determined by the strength and nature of the inter-protein interactions. Protein globules in these two samples have rather different intermolecular contacts. Microcrystals contain a large amount of solvent, protein globules are separated by a hydration layer, and they all have native (or very close to native) tertiary structure. In dehydrated amorphous powder, protein structures are distorted by unnatural both intra- and inter-molecular electrostatic interactions and hydrogen bonds network since solvent molecules do not saturate hydrophilic and H-bond sites.[18,19] One may therefore expect that the rocking motion parameters in these two samples are different, and we aimed to investigate this quantitatively.

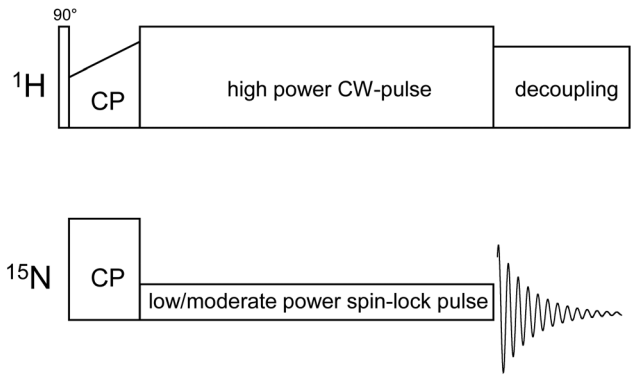

Fig. 1 Pulse sequence of the proton-decoupled ^{15}N $R_{1\rho}$ experiment.

Experimental details

Samples

Uniformly ^{15}N,^{2}H-enriched GB1 microcrystalline protein was purchased from Giotto Biotech, Italy. The sample packed in a 3.2 mm rotor was the same sample used in our previous work.[10] It contains ~20% of back-exchanged protons at labile sites. Partial back-exchange of labile protons is a compromise between suppressing proton-driven spin diffusion and keeping the NMR signal at a reasonable level. The lyophilized protein sample was prepared by dissolving ^{15}N,^{2}H-enriched protein (also purchased from Giotto Biotech) in a mixture of 20% H_2O–80% D_2O at a concentration of 5% by weight and subsequent lyophilization. The dissolution – lyophilization cycle was repeated twice. After that, the powder was packed in a 3.2 mm rotor and kept at room temperature under vacuum for three days to ensure the sample had minimum amount of water molecules. Then the rotor was sealed with a drive cap. The microcrystalline and amorphous samples were stored in a fridge at +5 C and −20 C, respectively.

NMR experiments

The experiments were conducted on a Bruker Avance 600 spectrometer using a 3.2 mm E-free MAS probe. Unlike our previous publication,[10] in this work, we observe the ^{15}N signal directly, without indirect proton detection. Proton detection has, of course, better signal-to-noise ratio, however, for the ^{15}N $R_{1\rho}$ experiment, it has the following disadvantage. The proton spectrum of the microcrystalline sample has two quite intensive peaks corresponding to residual solvent protons. These peaks are supposed to be suppressed by proper phase cycling. However, this suppression is not perfect; there are always certain distortions of the baseline around the solvent peaks. These distortions do not pose any problem if one aims at observing a spectrum. However, they hamper precise measurements of the signal intensity of the spectrum lines that are not far away from the solvent peaks. For different ^{15}N spin-lock pulse lengths, these distortions are not uniform; thus, they induce additional error scatter of ^{15}N $R_{1\rho}$ relaxation decays. This scatter nullifies the advantage of indirect proton detection. As for the lyophilized sample, there is no intensive solvent peak

in the proton spectrum, but the proton line is wider than the nitrogen one; again, we saw no significant advantage of indirect proton detection. On top of that, direct ^{15}N detection enables filtering out the Lys side chain peaks, which is impossible using 1D proton detection. In a few cases, we have compared the $R_{1\rho}$ decays measured using ^{15}N and ^{1}H detection, the decays look very similar, but ^{15}N detection provides a somewhat better signal-to-noise ratio. Thus, all the relaxation experiments presented below were conducted using the pulse sequence shown in Fig. 1. Prior to the repetition delay, we applied the compensating spin lock/decoupling pulse, the duration of which is a difference between the maximum spin-lock used in the experiments and the current spin-lock field (not shown in Fig. 1). This was done to keep the duty cycle the same for all durations of the spin-lock pulses.

The proton decoupling during the ^{15}N spin-lock pulse may cause additional sample heating, especially in samples with high ionic strength. Although this heating effect is not much different from that caused by proton decoupling during FID acquisition, it is advisable to control the sample temperature and/or to take measures against it. In our experiments, heating was practically negligible because of the usage of the E-free probe. The details of measuring the heating effect are presented in ESI.†

Fig. 2 shows 1D ^{15}N spectra for two samples. The powder spectrum reveals no narrow lines because proteins in the amorphous state have a distribution of conformations caused by inter-protein interactions, which leads to a heterogeneous distribution of chemical shifts. Since we look at the overall motion of protein globules, detection of 2D ^{15}N–^{1}H correlation site-resolved spectra is not helpful; for the lyophilized sample it is not possible anyway. Thus, all the experiments were conducted in 1D mode, and for plotting the relaxation decays, the integral intensity (area) of the spectrum in the range 95–140 ppm was used. All the $R_{1\rho}$ experiments were performed at a MAS rate of 18 kHz. The temperature calibration of the MAS probe was performed using a MAS rotor with methanol. Typical values of the experimental parameters: CP contact time 1.5 ms, ^{1}H $\pi/2$ pulse 2.8 μs, acquisition time 12 ms and 25 ms for the lyophilized and microcrystalline samples, respectively. ^{15}N spin-lock power was calibrated using the nutation experiment with proton decoupling during the ^{15}N pulse. Proton decoupling is necessary to avoid the influence of the ^{15}N–^{1}H dipolar coupling on the nutation curve. The spin-lock frequency must be calibrated as precise as possible since $R_{1\rho}$ dispersion curves may have a steep dependence, see below. While measuring standard $R_{1\rho}$ (*i.e.* without the proton irradiation during the ^{15}N spin-lock pulse), a ^{1}H π-pulse was applied in the middle of the ^{15}N spin-lock pulse. This was done to avoid the dipolar-CSA cross-correlation effect.[20]

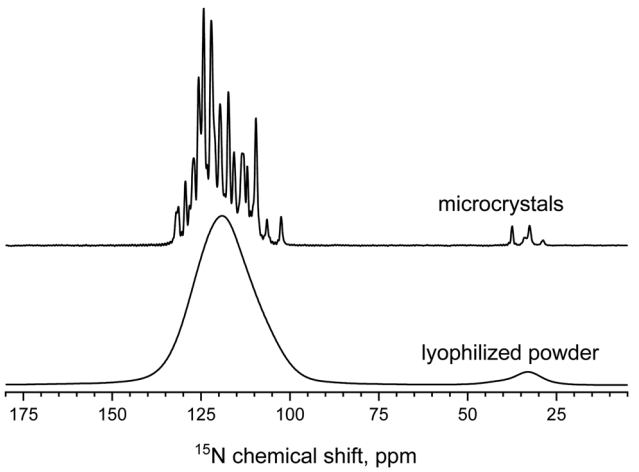

Fig. 2 ^{15}N CP MAS spectra of two GB1 samples. The processing was performed using Topspin software with Lorenzian line broadening of 20 Hz.

The motionally averaged ^{15}N–^{1}H dipolar couplings were measured using the R-PDLF sequence[21] under magic angle spinning of 10 kHz. The ^{1}H to ^{15}N magnetization transfer step was done using a cross-polarization transfer with a contact time of 50 μs. Such short CP time ensures that the interaction of only covalently bound ^{15}N–^{1}H pairs is observed. $R18^{7}_{1}$ recoupling blocks were used with π-pulses having a length of 5.55 microseconds. The indirect time increments used were equal to 22.22 microseconds; 64 points were measured in the indirect dimension. For the determination of the dipolar coupling, the dipolar modulation measured was Fourier transformed. The ^{15}N–^{1}H dipolar coupling was calculated by dividing the dipolar splitting obtained by the scaling factor 0.315. The projections of the 2D Fourier-transformed spectra for two samples and different temperatures are presented in the ESI.†

Numerical simulations

The numerical simulations of the ^{15}N $R_{1\rho}$ decays were performed using the Spinach software library for MATLAB.[22] It enables computationally efficient Liouville space simulations by using MATLAB's efficient handling of sparse matrices. Spinach's primary strength is to generate low-dimensional matrix representations for Liouville space operators and state vectors. This reduction of the problem dimension does not require extensive polynomial scaling of a computational cost with an increasing number of spins, which is a major advantage over *e.g.*, SIMPSON.

Our $R_{1\rho}$ simulation contains several loops over different parameters. From the inside out, they are iterated in the following order: first, the time domain is rasterized *via* the Spinach evolution() method. Second, the individual ^{15}N/^{13}C spin-lock and simultaneous ^{1}H decoupling pulses are simulated for every rotor period. Finally, the duration of the ^{1}H decoupling pulses and the power levels of the ^{15}N/^{13}C spin-lock and the ^{1}H decoupling pulses can be varied. The results are stored in the form of a multidimensional density matrix trajectory. For every set of parameters, the observable magnetization in the dependence of the spin-lock pulse duration was saved to an output file. The powder average is calculated *via* singlerot() in the lab frame, so the Fokker–Planck algorithm is utilized. A double-rotating frame transformation is performed for both spin types. Our code

enables not only CW ^{1}H decoupling but also rotor synchronised pulsing with variable number and duration of the pulses per one rotor period. In this work however, only the CW mode was used. The Spinach simulation is split into two separate files: one input and one simulation file. This has been done in accordance to Spinach simulation examples. The code is presented in the ESI.†

Data analysis

Relaxation decays

A remarkable feature of $R_{1\rho}$ relaxation decays is initial transient oscillations,[10,12] which appear if the spin-lock and local fields have comparable values. The nature of these oscillations can be explained qualitatively as follows. The local field components perpendicular to the spin-lock field cause precession of the magnetization vector around the spin-lock axis. Such precession manifests itself as oscillations on the relaxation decay. Under MAS, the amplitude of these oscillations increases upon approaching the rotary resonance condition (spin-lock and MAS frequencies are the same). This is illustrated by Fig. 3, which presents simulated relaxation decays at several spin-lock frequencies.

In the standard experiment (*i.e.* without ^{1}H decoupling), the amplitude of the oscillations increases as the difference between the MAS and spin-lock frequencies decreases. These oscillations comprise a "dead time" of the $R_{1\rho}$ decay. The mean relaxation rate of a multiexponential decay is the initial slope.[10,23] If the initial slope is hidden by the oscillations, it cannot be determined from an experimental decay. As demonstrated by the right panel of Fig. 3, proton decoupling almost completely suppresses these oscillations. Fig. 4 presents examples of the $R_{1\rho}$ decays measured with and without proton

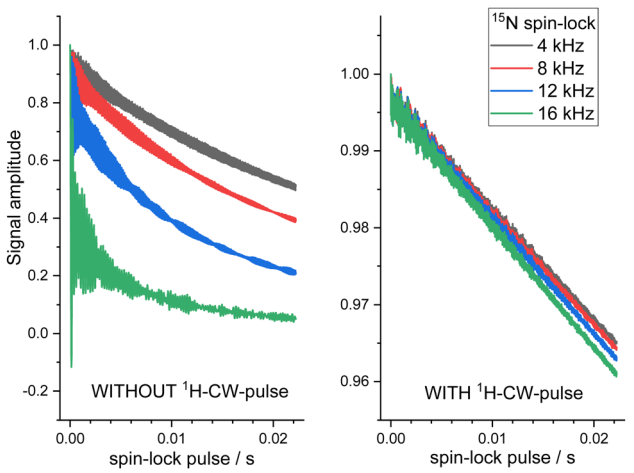

Fig. 3 Spinach-simulated ^{15}N $R_{1\rho}$ relaxation decays with and without 100 kHz ^{1}H CW-pulse during the ^{15}N spin-lock pulse. Parameters of the simulations: 2-site jumps of the ^{15}N–^{1}H vector with the angular amplitude 10°, correlation time 50 μs (jump rate 10^{4} s^{-1}), MAS rate 18 kHz, ^{15}N spin-lock frequencies are mentioned in the figure. Only the dipolar ^{15}N–^{1}H interaction was taken into account in the simulations.

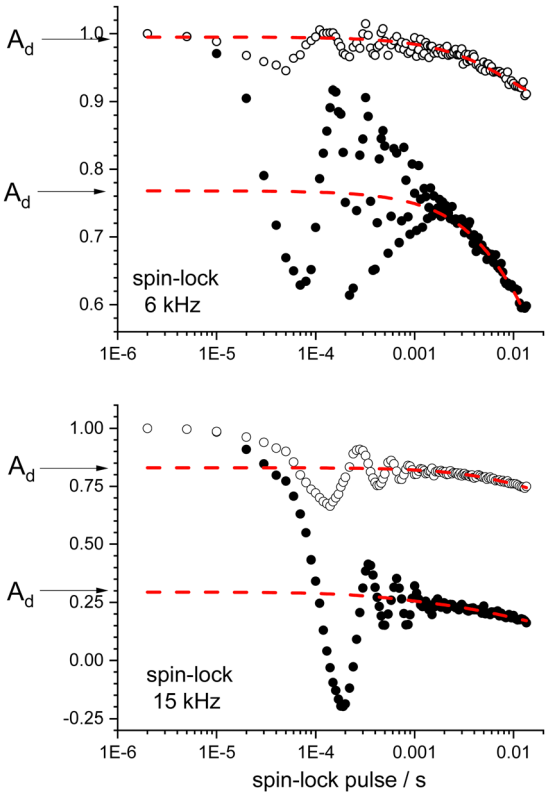

Fig. 4 Experimental $R_{1\rho}$ decays measured at two spin-lock fields for the microcrystalline sample at MAS rate 18 kHz. Open and solid symbols correspond to the experiments with and without ^{1}H decoupling, respectively. Dashed lines are the fitting curves extrapolated to short spin-lock delays. Parameter A_d defines the amplitude of the decay assuming that the first point (measured at the spin-lock duration 2 μs) is normalized to 1.

pulse during the ^{15}N spin-lock. Because of the B_1-field inhomogeneity, the initial oscillations of the experimental decays vanish much faster than those of the simulated ones.[10] Proton decoupling, as demonstrated by Fig. 4, also decreases the amplitude of the initial oscillations and hence, makes the "dead time" shorter. Still, it cannot suppress those entirely since it does not affect CSA.

Another significant effect of the proton decoupling is the increased normalized amplitude of the relaxation decay denoted in Fig. 4 as A_d. Fig. 5 shows the decay amplitude A_d as a function of the spin-lock field for the standard and proton-decoupled $R_{1\rho}$ experiments. It is seen that proton decoupling significantly increases the signal-to-noise ratio of the relaxation measurements, especially at small differences between the spin-lock and MAS frequencies. The initial oscillations and low decay amplitude prevent reliable $R_{1\rho}$ measurements at small difference $|\omega_{MAS} - \omega_{SL}|$ for the standard experiment. For this reason, we measured standard $R_{1\rho}$ up to the spin-lock 15 kHz that is, the minimum difference between MAS and spin-lock frequencies was 3 kHz. For the proton-decoupled experiment, we measured $R_{1\rho}$ up to the spin-lock 17 kHz. In this case, the difference $|\omega_{MAS} - \omega_{SL}|$ was three times less, which enables sampling significantly slower motions.

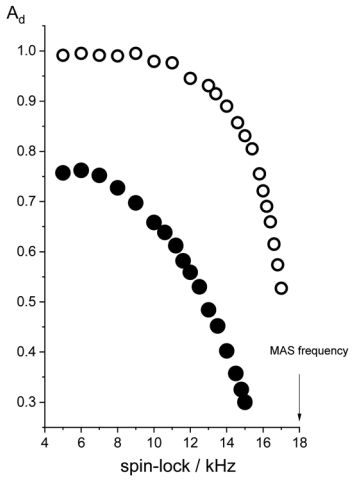

Fig. 5 Amplitude decay A_d (see Fig. 4) as a function of the spin-lock field for the standard (solid circles) and proton-decoupled (open circles) relaxation experiments. The experiments were performed on the lyophilized powder sample. The experimental error corresponds to the size of the circles.

Decreasing this frequency difference has decisive importance, as will be demonstrated below.

The mean relaxation rates $R_{1\rho}$ (*i.e.* the initial slope) were determined by fitting the decays using multi-exponential formula, the details are presented in ESI.†

Analytical formula for the hetero-nuclear dipolar relaxation mechanism of the proton-decoupled $R_{1\rho}$

The formulae for the dipolar and CSA relaxation mechanisms of the standard $R_{1\rho}$ rate were derived previously:[2,9,24]

$$R_{1\rho}^{\mathrm{dip}} = \frac{C_{\mathrm{NH}}{}^2}{60}[2J(\omega_{\mathrm{SL}} - 2\omega_{\mathrm{MAS}}) + 4J(\omega_{\mathrm{SL}} - \omega_{\mathrm{MAS}}) + 4J(\omega_{\mathrm{SL}} + \omega_{\mathrm{MAS}}) + 2J(\omega_{\mathrm{SL}} + 2\omega_{\mathrm{MAS}})] \quad (1)$$

$$R_{1\rho}^{\mathrm{CSA}} = \frac{(\delta\omega_{\mathrm{N}})^2}{135}[2J(\omega_{\mathrm{SL}} - 2\omega_{\mathrm{MAS}}) + 4J(\omega_{\mathrm{SL}} - \omega_{\mathrm{MAS}}) + 4J(\omega_{\mathrm{SL}} + \omega_{\mathrm{MAS}}) + 2J(\omega_{\mathrm{SL}} + 2\omega_{\mathrm{MAS}})] \quad (2)$$

where $C_{\mathrm{NH}}{}^2$ is the squared N–H dipolar coupling constant (for the N–H distance 1.02 Å it is equal to 5.2×10^9 s^{-2}), δ is the difference between parallel and perpendicular components of the CSA tensor, which for ^{15}N in a peptide bond is usually around 160 ppm, ω_{N} is a circular resonance frequency of ^{15}N nuclei. The terms containing spectral density functions at ^{15}N and ^{1}H resonance frequencies were omitted in eqn (1) and (2) since their contribution is negligible for systems with dynamics in the microsecond time scale.

The proton decoupling during spin-lock does not affect $R_{1\rho}^{\mathrm{CSA}}$, only $R_{1\rho}^{\mathrm{dip}}$, eqn (1), should contain one more parameter, the proton decoupling frequency ω_{H}. This formula was derived by us analytically; see details in ESI.† It looks as

$$R_{1\rho}^{\mathrm{dip}} = \frac{C_{\mathrm{NH}}{}^2}{60}[2J(\omega_{\mathrm{SL}} + \omega_{\mathrm{H}} + \omega_{\mathrm{MAS}}) + 2J(\omega_{\mathrm{SL}} + \omega_{\mathrm{H}} - \omega_{\mathrm{MAS}}) + J(\omega_{\mathrm{SL}} + \omega_{\mathrm{H}} + 2\omega_{\mathrm{MAS}}) + J(\omega_{\mathrm{SL}} + \omega_{\mathrm{H}} - 2\omega_{\mathrm{MAS}}) + 2J(\omega_{\mathrm{SL}} - \omega_{\mathrm{H}} + \omega_{\mathrm{MAS}}) + 2J(\omega_{\mathrm{SL}} - \omega_{\mathrm{H}} - \omega_{\mathrm{MAS}}) + J(\omega_{\mathrm{SL}} - \omega_{\mathrm{H}} + 2\omega_{\mathrm{MAS}}) + J(\omega_{\mathrm{SL}} - \omega_{\mathrm{H}} - 2\omega_{\mathrm{MAS}})] \quad (3)$$

It is seen that if $\omega_{\mathrm{H}} = 0$, then eqn (3) converts to eqn (1). Eqn (3) corresponds to the first part of eqn (S54) (ESI†) that is the spin-lattice relaxation of ^{15}N nuclei. In general, one has to consider the cross-relaxation rate between ^{15}N and ^{1}H (the second part of eqn (S54), ESI†). If the proton pulse is however much stronger than the ^{15}N spin-lock pulse and MAS rate ($\omega_{\mathrm{H}} \gg \omega_{\mathrm{SL}}, \omega_{\mathrm{MAS}}$), then the cross-relaxation rate is negligible, which directly follows from eqn (S53) (ESI†). Such inequality also prevents the cross-polarisation between ^{15}N and ^{1}H since the parameters ω_{H}, ω_{SL} and ω_{MAS} are far away from the Hartmann–Hahn match condition. In our experiments, we always kept $\omega_{\mathrm{H}}/2\pi$ equal to 100 kHz.

To check the validity of eqn (3), we performed Spinach simulations of the proton-decoupled $R_{1\rho}$ experiment. Fig. 6 compares analytical (eqn (3)) and numerical simulations of the relaxation rate $R_{1\rho}^{\mathrm{dip}}$ as a function of the motional correlation time. The spectral density function in the analytical calculations (eqn (3)) was used in the form

$$J(\omega) = (1 - S^2)\frac{\tau}{1 + (\omega\tau)^2} \quad (4)$$

where S^2 and τ are the motional order parameter and correlation time, respectively. The correspondence between the numerical

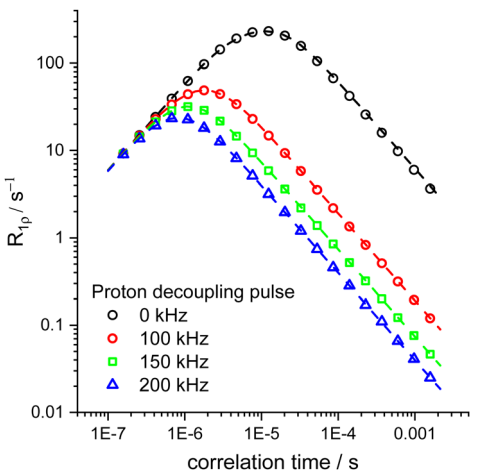

Fig. 6 Comparison of the analytical (eqn (3), dashed curves) and Spinach-simulated (symbols) dipolar relaxation rates at different strengths of the proton decoupling pulse (indicated in the figure) and correlation times. Numerical simulations were performed for the two-site jumps of the ^{15}N–^{1}H vector. The angle between two directions (sites) of the ^{15}N–^{1}H vector 16°, this corresponds to the order parameter S^2 = 0.943. MAS 18 kHz, ^{15}N spin-lock 8 kHz, ^{15}N–^{1}H distance 1.02 Å.

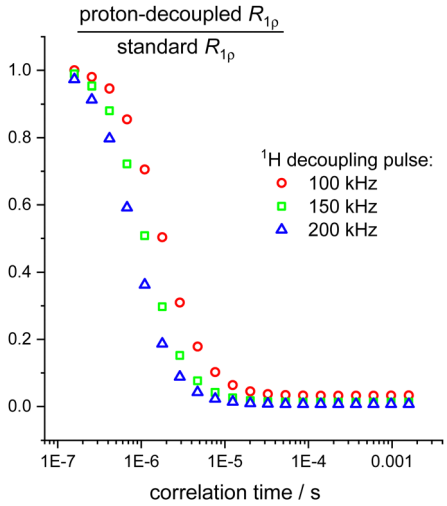

Fig. 7 The ratio of the proton-decoupled $R_{1\rho}$ to the standard $R_{1\rho}$ as a function of the correlation time. The Spinach-simulated relaxation rate values are taken from Fig. 6.

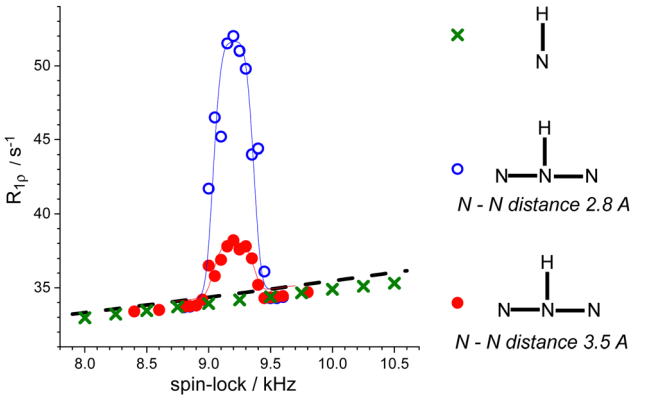

Fig. 8 ^{15}N dipolar $R_{1\rho}$ (without proton decoupling) simulations as function of the spin-lock frequency in the vicinity of the HORROR condition. Dashed line – analytical simulation using eqn (1) and spectral density in the form of eqn (4), symbols – Spinach simulations, that were performed for three different nuclei systems indicated in the figure. N–H distance in all cases was 1.02 Å. Parameters of the simulations: MAS 18 kHz, 2 site jumps with the angular amplitude 6° (S^2 = 0.9918) and correlation time 10.8 μs. 4-Nuclei systems are assumed to be rigid, during the jumps, they rotate as a whole around the axis perpendicular to the plane of the structures. In the 4-nuclei systems, the signal of only central ^{15}N nucleus was observed. Thin lines indicate the phenomenological description of the HORROR peak as described in the text.

simulations and the analytical model is rather good. An important consequence of these simulations is shown in Fig. 7. One may see that high power proton decoupling during ^{15}N spin-lock pulse effectively "switches off" the dipolar relaxation mechanism for slow motions, and it has no effect for fast motions. Thus, from a simple comparison of the standard and proton-decoupled $R_{1\rho}$'s measured at the same ^{15}N spin-lock one may unambiguously determine a (non)presence of a slow motion in a sample. Moreover, if the motional correlation time is comparable to the inverse value of the proton decoupling frequency, then at a first approximation, it can be determined just from the ratio of the relaxation rates, as it follows from Fig. 7.

HORROR and B_1 field inhomogeneity

It is already known that while measuring ^{15}N $R_{1\rho}$ in proteins under MAS, one has to avoid the so-called HORROR condition[25] that occurs when spin-lock frequency equals half of the MAS frequency.[3,10] At this condition, the homonuclear ^{15}N–^{15}N dipolar interaction is recoupled. This interaction is too weak compared to the ^{15}N–^{1}H coupling and does not contribute to the relaxation rate. However, it induces similar oscillations in the initial part of the relaxation decay as the ones considered above. Since the amplitude and the frequency of these oscillations are small, they extend to longer times increasing the "dead time" of the decay. To quantify this effect, we conducted Spinach $R_{1\rho}$ relaxation simulations in the vicinity of the HORROR condition for the ^{15}N–^{1}H spin pair and for a system of four nuclei, one ^{1}H and three ^{15}Ns. The results of these simulations are shown in Fig. 8.

As it is seen, at typical ^{15}N–^{15}N distances in a polypeptide chain, the ^{15}N–^{15}N dipolar coupling causes the appearance of a spurious narrow peak in the $R_{1\rho}$ dispersion at the HORROR condition. An analytical description of this peak is hardly possible since the determination of the initial slope (*i.e.* mean relaxation rate) from fitting a slowly oscillating decaying function is uncertain. Thus, the relaxation rates within the HORROR point vicinity may have only approximate values and cannot be attributed to the relaxation itself. These values are distorted, and they should not be analysed in terms of dynamic parameters. We described the HORROR peak (shown by thin solid lines in Fig. 8) by a phenomenological function

$$R_{1\rho}^{\mathrm{HORROR}}(\nu_{\mathrm{SL}}) = H \cdot \exp\left[-0.5 \cdot \left(\frac{\nu_{\mathrm{SL}} - 9.2\,\mathrm{kHz}}{0.15\,\mathrm{kHz}}\right)^4\right] \quad (5)$$

where H is a variable peak amplitude. Fig. 8 shows that the top of the $R_{1\rho}$ peak is shifted approximately 200 Hz from the exact HORROR condition. We do not know the reason for this; most probably, this is just the uncertainty of fitting the initial slope of the decay. Anyhow, the main result of these simulations is an indication that the HORROR $R_{1\rho}$ peak is relatively narrow, and that outside the range ~300 Hz from its top, the interfering effect of the ^{15}N–^{15}N coupling is negligible.

The experimental data (Fig. 9) also reveal the HORROR peak, but it is much wider than in the case of the numerical simulations. The source of this discrepancy is readily understood if one considers the RF field inhomogeneity. In practice, a single $R_{1\rho}$ experiment will never relate to a single spin-lock frequency but to a distribution that depends on the coil and the occupied volume by the sample in the rotor. To describe the $R_{1\rho}$ dispersion in this case, one needs to use the distribution function:

$$R_{1\rho}^{*}(\nu_{\mathrm{SL}}) = \int_{\min}^{\max} R_{1\rho}(\nu) P_{\mathrm{inhom}}(\nu_{\mathrm{SL}}, \nu) \mathrm{d}\nu \quad (6)$$

where $R_{1\rho}^{*}(\nu_{\mathrm{SL}})$ is the mean relaxation rate averaged over a distribution of the spin-lock frequencies, $R_{1\rho}(\nu)$ is the sum of the rates determined by eqn (2), (3) and (5), $P_{\mathrm{inhom}}(\nu_{\mathrm{SL}},\nu)$ is the

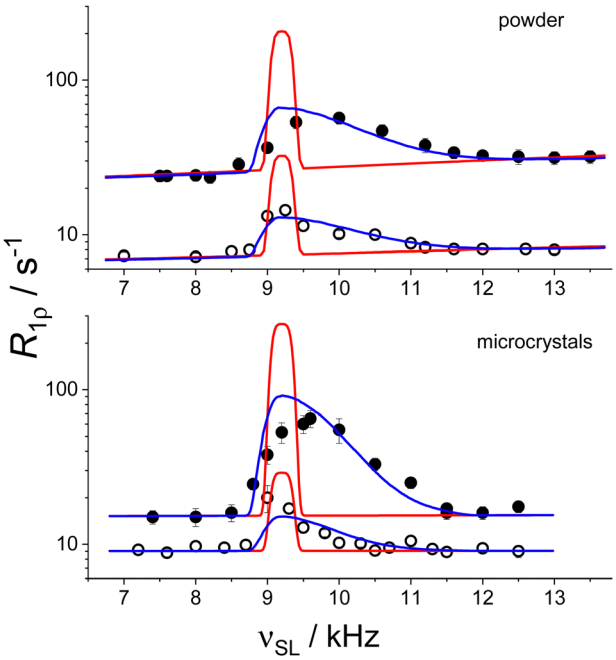

Fig. 9 Experimental $R_{1\rho}$ dispersions measured in two GB1 samples within the vicinity of the HORROR condition. Solid and open symbols – standard and proton-decoupled (proton decoupling 100 kHz) $R_{1\rho}$ rates, respectively. Red lines – simulated dispersions assuming no B_1 inhomogeneity. These curves were calculated using eqn (1) and (5). Spectral density function in eqn (1) was used in the form of eqn (4), order parameter and the correlation time were adjusted so that the simulated lines coincide with the experimental data on the edges of the HORROR peaks. Blue lines – dispersions simulated using eqn (6). The height of the HORROR peak (parameter H in eqn (5)) was adjusted to achieve the best coincidence between the experimental and the simulated data.

function describing the distribution of the spin-lock frequencies at a certain mean spin-lock frequency ν_{SL}. From Fig. 9 it is seen that the distribution function $P_{\text{inhom}}(\nu_{SL},\nu)$ is highly asymmetric. To describe the data in Fig. 9, we used the truncated Gaussian distribution function, *i.e.* we assumed the integration limits "min" and "max" in eqn (6) to be unequally spaced with respect to ν_{SL}. Then the distribution function can be expressed as

$$P_{\text{inhom}}(\nu_{SL},\nu) = \frac{1}{N}\exp\left(-\frac{(\nu_{SL}-\nu)^2}{2(k\cdot\nu_{SL})^2}\right) \quad (7)$$

where N is the normalization coefficient and k is the parameter that determines the distribution width of this distribution function. The absolute value of the distribution width of the spin-lock frequencies should obviously be proportional to the mean spin-lock frequency. That is why sigma, a distribution width parameter in the Gaussian function in eqn (7), is a product $(k\cdot\nu_{SL})$. For two samples, protein powder and protein microcrystals, we tried to find the parameters "min", "max" and "k" to describe the shape of the experimental HORROR peak. These numbers are summarized in Table 1 and are in line with the RF inhomogeneity profiles reported previously.[26,27]

Table 1 Parameters of eqn (6) and (7) describing the shape of the HORROR peak in two protein samples, Fig. 9

	Min	Max	k
GB1 powder	$\nu_{SL}(1-3k)$	$\nu_{SL}(1+0.3k)$	0.1
GB1 microcrystals	$\nu_{SL}(1-3k)$	$\nu_{SL}(1+0.4k)$	0.07

It is seen that the spin-lock frequency distribution for the two samples is somewhat different. This looks reasonable since the B_1 inhomogeneity depends not only on the geometry of a coil in a probe, but also on the volume and location of a sample inside the rotor. In our case, the samples were slightly different: the powder sample occupied the whole inner volume of the MAS rotor, while the microcrystalline sample was packed in the rotor with spacers that limited its volume. Thus, slightly different distribution functions for these samples can be explained.

One may ask, why do we need to describe the HORROR peaks whereas these data should be excluded from the analysis anyway? The answer is: we need to use the inhomogeneity distribution function while fitting the whole $R_{1\rho}$ dispersion. This necessity is demonstrated by Fig. 10, which compares simulated $R_{1\rho}$ dispersions using eqn (1) and (6) for different motional correlation times. If the correlation time is relatively short, then the $R_{1\rho}$ dispersions are flat and including B_1 inhomogeneity in the analysis is not necessary. However, when the motional correlation time has a value around few hundred microseconds, the dispersion becomes very nonlinear and steep. Neglecting the B_1 inhomogeneity may result in an error up to 40%, especially at small differences between the spin-lock and MAS frequencies. Thus, HORROR is an interfering effect; however, it helps determining the B_1 inhomogeneity

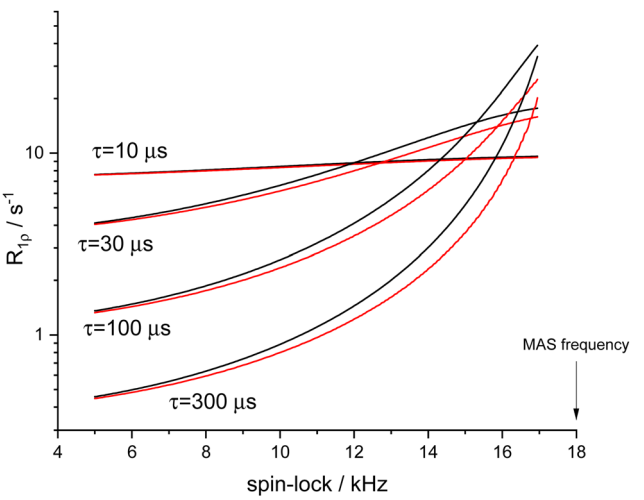

Fig. 10 Simulated $R_{1\rho}$ dispersions for different motional correlation times assuming no B_1 inhomogeneity (black lines) and B_1 inhomogeneity distribution function for the powder sample (red lines), see details in the text. These curves were calculated using eqn (1) and (6), respectively, the spectral density function was assumed to be in the form of eqn (4). The order parameter can be chosen arbitrarily since it only shifts the whole plot in a vertical direction.

distribution function, which is necessary for the correct quantitative analysis of the relaxation data in the whole range of spin-lock frequencies. Measuring the HORROR $R_{1\rho}$ peak should hardly be a routing procedure for determining the B_1 field distribution function, this can be done in a less time-consuming way, see *e.g.* ref. 28. We measured the HORROR peak in detail first of all for visual demonstration of the HORROR effect on the $R_{1\rho}$ rates and typical range of the spin-lock frequencies that should be avoided while measuring $R_{1\rho}$ dispersions.

Results and discussion

Fig. 11 shows the $R_{1\rho}$ dispersions measured for two samples at three temperatures. For both samples, the HORROR peak was measured only at T = 19 °C; at two other temperatures, the relaxation rates within the range from 8 to 12 kHz were not measured.

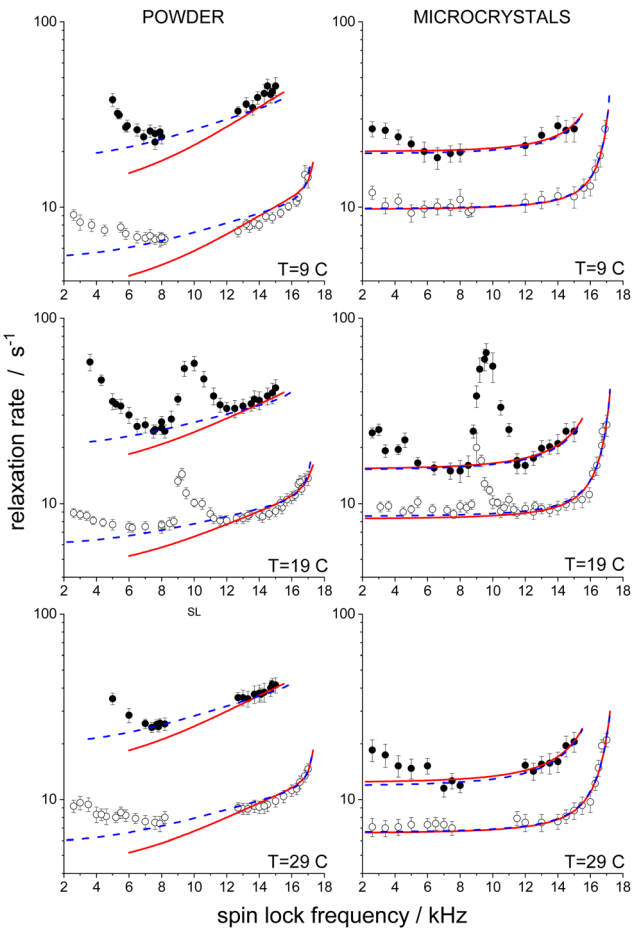

Fig. 11 $R_{1\rho}$ dispersions measured for two samples at three temperatures (indicated in the figure). Solid and open circles are the standard and proton-decoupled relaxation rates, respectively. Solid red lines are the fitting curves obtained from the fitting the rates at spin-lock frequencies above 12 kHz. Dashed blue lines are the fitting curves obtained from fitting the rates at ν_{SL} > 12 kHz and 6.5 kHz < ν_{SL} < 8.2 kHz (see details in the text).

Spin-spin and Bloch–McConnell contributions to the relaxation rates

Before presenting the fitting results, we would like to discuss the observed $R_{1\rho}$ decrease with increasing spin-lock frequency at small values of the latter (Fig. 11). Such a decrease cannot be reproduced using eqn (1)–(3). Only two mechanisms can be responsible for this behaviour: Bloch–McConnell dispersion[29] and spin–spin (coherent) contribution to the relaxation rate $R_{1\rho}$ mentioned in the Introduction. The Bloch–McConnell contribution to the relaxation rate is the relaxation mechanism due to the modulation of the isotropic chemical shift by conformational transitions of molecules. This is one of the standard approaches to observe slow molecular dynamics in liquids[30,31] and in solids.[7,32–34] Spin–spin contribution is a relaxation of ^{15}N nuclei over proton dipole–dipole reservoir to the lattice; it becomes significant only at low spin-lock fields. The limiting step in this relaxation pathway is the cross-relaxation rate between nitrogens and protons. Coherent contribution is an interfering effect since it provides no information about molecular dynamics and hides the incoherent contribution to the relaxation rate. There were some attempts to take it into account[35] or to suppress it using homonuclear proton decoupling,[36] proton isotopic dilution,[37] and conducting the experiments at high MAS rates.[38] None of these approaches, however, appeared to be robust and applicable at all values of the spin-lock field. The proton-decoupled $R_{1\rho}$ experiment solves this problem in the best way. Since proton decoupling disrupts the connection between protons and nitrogens, the cross-relaxation rate becomes negligibly small, and thus, the interfering spin–spin contribution can be suppressed completely.

Fig. 11 demonstrates that the $R_{1\rho}$ dispersions at small spin-lock frequencies for the standard and proton-decoupled experiments are quite different. For the standard experiment, the $R_{1\rho}$ *vs.* ν_{SL} dependence is appreciably steeper than that for the proton-decoupled one. As discussed above, the standard $R_{1\rho}$ is sensitive to both Bloch–McConnell and spin–spin contributions, whereas the proton-decoupled $R_{1\rho}$ can only be affected by the Bloch–McConnell mechanism. From this, we may draw two conclusions.

First, if high MAS rates are not used, the interfering spin–spin relaxation mechanism can affect standard $R_{1\rho}$ rates at small spin-lock fields even in proton-diluted protein samples. The ratio between the spin–spin and spin–lattice contributions to $R_{1\rho}$ at small spin-lock fields is determined by proton density in a sample, MAS rate and motional parameters. The estimation of this ratio *a priori* is not possible in all cases; this is however easy to do using the comparison of the standard and proton-decoupled $R_{1\rho}$ dispersions. Note that the proton-decoupled $R_{1\rho}$ experiment makes possible measuring Bloch–McConnell dispersions even in fully protonated samples.

One may see that the spin–spin contribution in the powder sample is more significant than in the microcrystalline sample. This most reasonably can be explained by a different proton density in the samples. We tried to keep the back-exchange

fraction of protons in both samples the same; this, however, seems to be not the case. We could not completely avoid contact of the powder sample with atmospheric vapour during the sample preparation, and/or probably, the deuteration of the two samples was somewhat different, or there were some other unknown to us reasons affecting the amount of protons in the samples. In any case, for the proton-decoupled experiment, all this plays no role.

Second, the powder and microcrystalline samples reveal different proton-decoupled $R_{1\rho}$ dispersions at small spin-lock frequencies: in the powder sample, one may observe the $R_{1\rho}$ decrease upon increasing spin-lock frequency whereas in the microcrystalline sample, the dispersions are nearly flat. In the proton-decoupled experiment, such dispersion can be attributed to the Bloch–McConnell mechanism only, which unambiguously signifies slow conformational dynamics of a protein structure. The Bloch–McConnell dispersions in the microcrystalline GB1 sample measured previously using site-selective 2D-mode of the $R_{1\rho}$ experiment[5] have shown that two segments of the protein structure undergo slow conformational transitions. This does not contradict to our data since we measure the integral signal from the whole protein. Only 18 out of 56 residues in GB1 reveal appreciable Bloch–McConnell dispersions[5] and thus, the dispersion step in the 1D-experiment can be barely visible. The powder sample, however, shows noticeable Bloch–McConnell dispersion (Fig. 11, left panel), which directly points to more significant conformational dynamics. This can hardly be an inherent internal dynamics since in the dehydrated state, all the conformational protein motions can be only suppressed, but not enhanced.

We suggest the following explanation of the difference between the Bloch–McConnell dispersions in the powder and microcrystalline samples. The dispersion in the frequency range of a few kHz corresponds to a motional correlation time of the order of few hundred microseconds. This value corresponds to the correlation time of one of the components of the rocking motion correlation functions (see below). This coincidence may indicate that the rocking motion is accompanied by conformational changes of a protein structure. We suppose this is bending/twisting a protein globule upon rocking motion. Proteins in dry powder are tied to each other by a variety of inter-globular contacts (hydrogen bonds and sterical hindrances). Thus, it is difficult to imagine that they can undergo a motion as a whole as stiff, rigid bodies without any structural deformations. In the crystalline state, inter-protein contacts are weaker, proteins are separated by a solvent layer and there are no unnatural inter-globular hydrogen bonds. Hence, proteins in a crystal may move more independently from each other. Thus, their rocking motion is accompanied by much smaller structural deformations, if at all, than protein molecules in the dry powder sample. To prove or disprove this hypothesis, obviously more experimental data are needed.

Rocking motion parameters

Now let us consider the results of fitting the relaxation rates. The fitting parameters were obtained using eqn (6) and the distribution function parameters presented in Table 1. Since the HORROR peak data were excluded from fitting, we did not include the HORROR contribution (eqn (5) and eqn (6); the relaxation rate $R_{1\rho}(\nu)$ under the integral in eqn (6) was a sum of $R_{1\rho}^{\mathrm{CSA}}$ (eqn (2)) and $R_{1\rho}^{\mathrm{dip}}$ (eqn (3)) only. Using these equations, we may fit only the $R_{1\rho}$'s measured at the spin-lock frequencies above 12–12.5 kHz (see Fig. 11). It is unclear if the rates measured at the frequencies between 6.5–7 and 8–8.2 kHz can be included in the fitting. This range of the spin-lock frequencies corresponds to the minimum between the Bloch–McConnell dispersion and the HORROR peak (Fig. 11). We are not sure whether the Bloch–McConnell contribution to the relaxation rate is negligible at this point or not. For this reason, we performed the fitting, including and excluding the rates measured between 6.5 and 8.2 kHz.

Before fitting, one has to assume a correlation function model. The simplest single exponential correlation function (the spectral density has a form of eqn (4)) cannot describe the data adequately since the discrepancy between the experimental data and fitting curves was too large. Distribution of the correlation times (Gaussian or log-normal) could not significantly improve the fitting quality. We could fit the data reasonably well only if we assume two different components of the correlation function with very different correlation times. In this case, the spectral density function has the form:

$$J(\omega) = \left(1 - S^2\right)\left[A\frac{\tau_{\mathrm{F}}}{1 + (\omega\tau_{\mathrm{F}})^2} + (1 - A)\frac{\tau_{\mathrm{S}}}{1 + (\omega\tau_{\mathrm{S}})^2}\right] \qquad (8)$$

where τ_{F} and τ_{S} are the correlation times of the fast and slow components, and A is the relative amplitude of the fast component of the rocking motion correlation function. It should be mentioned that this form of the spectral density function is also a simplification of an actual physical picture. Most probably, these two components also have correlation times distributions, and there are some indications of this, as will be discussed below. The distributions, however, do not improve the fitting quality but make the fit more uncertain since we need to introduce additional fitting parameters. Thus, we limited ourselves to only four fitting parameters (S^2, τ_{F}, τ_{S} and A) and used the spectral density function in the form of eqn (8). To fit the data, one also needs to know the values of ${C_{\mathrm{NH}}}^2$ and δ (see eqn (1) and (2)) averaged by the fast conformational motions. We therefore measured ${C_{\mathrm{NH}}}^2$ experimentally obtaining the values 4.35×10^9 s^{-2} and 3.9×10^9 s^{-2} for the powder and microcrystalline samples, respectively (see Fig. S4 of the ESI†). Since the residual dipolar coupling reveals no visible temperature dependence for both samples, these values were used for all temperatures. The ratio of these values to the rigid lattice value (5.2×10^9 s^{-2}) provides the mean order parameter of the fast backbone motions, which is 0.836 and 0.75, respectively. We did not measure motional averaging of the CSA tensor; we could, however, reasonably assume that CSA is being averaged to the same extent as N–H dipolar coupling. The rigid lattice value of δ is 160 ppm; thus, the motionally averaged values are 160 ppm $\cdot \sqrt{0.836} = 146$ ppm and 160 ppm $\cdot$

Table 2 The values of the correlation function parameters obtained from the fitting the $R_{1\rho}$ dispersions at three temperatures for two fitting options (see details in the text)

T/°C	S^2	A	τ_F/μs	τ_S/ms
Powder sample				
$R_{1\rho}$ measured at $\nu_{SL} > 12$ kHz				
9	0.9929 ± 0.0018	0.727 ± 0.13	23.88 ± 1.2	1.2 ± 1.0
19	0.9936 ± 0.0007	0.811 ± 0.07	18.65 ± 1	0.43 ± 0.3
29	0.992 ± 0.0022	0.698 ± 0.13	20.2 ± 1	1.35 ± 1.15
Powder sample				
$R_{1\rho}$ measured at 6.5 kHz $< \nu_{SL} <$ 8.2 kHz and $\nu_{SL} > 12$ kHz				
9	0.9918 ± 0.0025	0.697 ± 0.13	15.55 ± 0.5	0.85 ± 0.82
19	0.9931 ± 0.0007	0.819 ± 0.05	12.8 ± 0.5	0.28 ± 0.22
29	0.9917 ± 0.002	0.727 ± 0.11	14.7 ± 0.35	0.89 ± 0.73
Microcrystalline sample				
$R_{1\rho}$ measured at $\nu_{SL} > 12$ kHz				
9	0.971 ± 0.012	0.32 ± 0.1	2.68 ± 0.07	1.58 ± 0.73
19	0.983 ± 0.004	0.442 ± 0.07	2.2 ± 0.08	0.7 ± 0.27
29	0.989 ± 0.009	0.525 ± 0.04	2.24 ± 0.08	0.44 ± 0.085
Microcrystalline sample				
$R_{1\rho}$ measured at 6.5 kHz $< \nu_{SL} <$ 8.2 kHz and $\nu_{SL} > 12$ kHz				
9	0.975 ± 0.01	0.363 ± 0.1	2.52 ± 0.06	1.38 ± 0.85
19	0.982 ± 0.005	0.446 ± 0.08	2.02 ± 0.07	0.77 ± 0.34
29	0.989 ± 0.007	0.556 ± 0.03	2.03 ± 0.06	0.39 ± 0.07

$\sqrt{0.75} = 138.5$ ppm for the powder and microcrystalline samples, respectively. So, in the fitting procedure, we used these values of the coupling constants. The values of the fitting parameters are presented in Table 2. Fitting was performed using the Monte–Carlo algorithm, as done in our previous work.[10]

Several features of the obtained results have to be mentioned. First, the inclusion or exclusion of the relaxation rates measured at frequencies below the HORROR peak affects the results for only the powder sample. Even for the powder sample, the difference is not dramatic. We believe that fitting the rates measured for this sample only at $\nu_{SL} > 12$ kHz is more relevant since (a) it provides better fitting quality and (b) the Bloch–McConnell contribution seems to be relatively large, unlike the microcrystalline sample, and one may expect that it is still significant at spin-lock frequencies around 7–8 kHz.

Second, the accuracy of various fitting parameters is different. The most accurately determined parameter is τ_F. Its value is determined primarily by the ratio of the standard and proton-decoupled $R_{1\rho}$'s, see Fig. 7. This demonstrates the advantage of the simultaneous analysis of these two types of the relaxation rates; proton-decoupled $R_{1\rho}$ dispersions alone would not be as informative. The least precise value is τ_S. The information about the slow correlation function component is contained only in the proton-decoupled $R_{1\rho}$'s measured at small frequency difference ($\nu_{MAS} - \nu_{SL}$), namely in the strong $R_{1\rho}$ raising up upon approaching the spin-lock frequency to the MAS point (Fig. 11). This frequency range is inaccessible for the standard $R_{1\rho}$'s, and it is clear that without the proton-decoupled data, the slow component of the rocking motion would not be detected at all. At the same time, these data are difficult to measure precisely because of the initial oscillations. In addition, even a small miscalibration of the spin-lock frequency at small ($\nu_{MAS} - \nu_{SL}$) may lead to a significant error in the analysis. We also would like to add that the fitting parameters τ_S and A have very strong inter-correlation. Fixing one of these parameters during fitting significantly reduces the fitting uncertainty of the other one.

Third, as mentioned above, while fitting the data we assumed no correlation times distributions, which is an obvious simplification of molecular dynamics in such complex system. Our data do not allow unambiguous determination of the correlation times distribution function. Still, there are some indications that the distributions do exist. First, one may see that both samples reveal very weak, if at all, temperature dependence of the motional correlation times, except τ_S in the microcrystalline sample. This seems to be strange, but this can be explained by distributions of the correlation times. The distributions conceal visible temperature dependence, which cannot be experimentally observed within a narrow temperature range. Second, there is an unexpected temperature dependence of the order parameter of the fast motion in the microcrystalline sample: the order parameter increases from 0.975 (T = 9 °C) to 0.989 (T = 29 °C), see Table 2, which means that the amplitude of the rocking motion decreases roughly twice with increasing temperature. Such unnatural apparent behaviour can also be explained by introducing the distribution function for the correlation time τ_F. The details of this analysis is presented in ESI.† The slow component probably also has correlation time distribution; on the other hand, this distribution should not be very wide since GB1 and SH3 proteins in crystal form undergo no rocking motion in the millisecond time scale.[39]

Fourth, the most important conclusion is that the rocking motion parameters for microcrystalline and powder samples differ. The motional amplitude is appreciably higher for microcrystals than for amorphous powder. This is reasonable since proteins in powder have tighter and stronger inter-molecular contacts. This is in line with the previous studies of another protein, ubiquitin, which has different rocking motion amplitudes in two different crystal packings.[10,15] As for the bimodal form of the rocking motion correlation function, the available data are not sufficient for its unambiguous physical interpretation. It is natural to suppose that the fast component corresponds to the wobbling of individual proteins, which is independent from neighbours, and the slow mode of the correlation function reflects collective motions of large protein assemblies. This is, however, only speculations. More abundant data obtained for different proteins and at different conditions are necessary to ascribe the correlation function components to specific physical processes, which is our plan for future studies.

Conclusions

High-power proton decoupling during the ^{15}N spin-lock pulse in the $R_{1\rho}$ experiment provides several significant methodological advantages that make the experiment more reliable, precise and informative. The most important advantage is that the proton decoupling enables measuring $R_{1\rho}$ rates at a much smaller difference between the spin-lock and MAS frequencies,

thus making possible to observe much slower molecular motions. The experimental HORROR peak in the $R_{1\rho}$ dispersions, which corresponds to the condition of recoupling the homonuclear ^{15}N–^{15}N dipolar interaction, is wider than in the case of numerical simulations because of the B_1 field inhomogeneity. This is an interfering effect; on the other hand, it may help to determine the B_1 field inhomogeneity distribution function.

Studying protein rocking motion in two solid samples by $R_{1\rho}$ relaxometry has demonstrated that the simultaneous analysis of both standard and proton-decoupled relaxation rates provides the most exact results. Still, we do not overestimate the accuracy of the obtained values of the dynamic parameters since the data treatment is associated with some assumptions and uncertainties. Despite that, the $R_{1\rho}$ data analysis enables drawing several important qualitative conclusions on the nature of the protein rocking motion. The rocking motion properties depend on the strength and nature of the inter-protein contacts. In lyophilized powder, the inter-protein interactions are more tight and abundant than in microcrystals; thus, the rocking motion amplitude in the powder sample must be smaller, which is demonstrated by our data. There is an indication of a possible bending/twisting of protein globules, which accompanies rocking motion in the powder sample. This follows from the analysis of the Bloch–McConnell parts of the $R_{1\rho}$ dispersions; however, this supposition still needs to be confirmed. The most surprising result is that the rocking motion correlation function consists of two components with correlation times of around a few microseconds and hundreds of microseconds. However, the physical nature of such a form of the correlation function is not yet clear.

Conflicts of interest

There are no conflicts to declare.

Acknowledgements

Prof. Kay Saalwächter is thanked for his constant and comprehensive support of this project. This research was supported by the Deutsche Forschungsgemeinschaft, grant number KR 3033/1-1.

References

1 E. G. Keeler and A. McDermott, *Chem. Rev.*, 2022, **122**, 14940–14953.
2 P. Rovo, *Sol. State Nucl. Magn. Reson.*, 2020, **108**, 101665.
3 L. Vugmeister, D. Ostrovsky, A. Greenwood and R. Fu, *J. Magn. Reson.*, 2022, **337**, 107171.
4 P. Rovo, C. A. Smith, D. Gauto, B. L. de Groot, P. Schanda and R. Linser, *J. Am. Chem. Soc.*, 2019, **141**, 858–869.
5 C. Öster, S. Kosol and J. R. Lewandowski, *Sci. Rep.*, 2019, **9**, 11082.
6 A. A. Smith, M. Ernst, S. Riniker and B. H. Meier, *Angew. Chem., Int. Ed.*, 2019, **131**, 9483–9488.
7 P. Schanda and M. Ernst, *Prog. Nucl. Magn. Reson. Spectrosc.*, 2016, **96**, 1–46.
8 U. Haeberlen and J. S. Waugh, *Phys. Rev.*, 1969, **185**, 421–429.
9 R. Kurbanov, T. Zinkevich and A. Krushelnitsky, *J. Chem. Phys.*, 2011, **135**, 184104.
10 A. Krushelnitsky, D. Gauto, D. C. R. Camargo, P. Schanda and K. Saalwächter, *J. Biomol. NMR*, 2018, **71**, 53–67.
11 A. Krushelnitsky, R. Kurbanov, D. Reichert, G. Hempel, H. Schneider and V. Fedotov, *Sol. State Nucl. Magn. Reson.*, 2002, **22**, 423–438.
12 D. L. VanderHart and A. N. Garroway, *J. Chem. Phys.*, 1979, **71**, 2773–2787.
13 A. Krushelnitsky, D. Faizullin and D. Reichert, *Biopolymers*, 2004, **73**, 1–15.
14 A. Krushelnitsky and D. Reichert, *Appl. Magn. Reson.*, 2004, **27**, 501–518.
15 P. Ma, Y. Xue, N. Coquelle, J. D. Haller, Z. Yuwen, I. Ayala, O. Mikhailovskii, D. Willbold, J.-P. Colletier, N. Skrynnikov and P. Schanda, *Nat. Commun.*, 2015, **6**, 8361.
16 J. M. Lamley, C. Oster, R. A. Stevens and J. R. Lewandowski, *Angew. Chem., Int. Ed.*, 2015, **51**, 15374–15378.
17 V. Kurauskas, S. A. Izmailov, O. N. Rogacheva, A. Hessel, I. Ayala, J. Woodhouse, A. Shilova, Y. Xue, T. Yuwen, N. Coquelle, J.-P. Colletier, N. R. Skrynnikov and P. Schanda, *Nat. Commun.*, 2017, **8**, 145.
18 J. A. Rupley and G. Careri, *Adv. Protein Chem.*, 1991, **41**, 37–172.
19 K. Griebenow and A. M. Klibanov, *Proc. Natl. Acad. Sci. U. S. A.*, 1995, **92**, 10969–10976.
20 V. Kurauskas, E. Weber, A. Hessel, I. Ayala, D. Marion and P. Schanda, *J. Phys. Chem. B*, 2016, **120**, 8905–8913.
21 S. V. Dvinskikh, H. Zimmermann, A. Maliniak and D. Sandström, *J. Magn. Reson.*, 2004, **168**, 194–201.
22 H. J. Hogben, M. Krzystyniak, G. T. P. Charnock, P. J. Hore and I. Kuprov, *J. Magn. Reson.*, 2011, **208**, 179–194.
23 D. A. Torchia and A. Szabo, *J. Magn. Reson.*, 1982, **49**, 107–121.
24 A. Krushelnitsky, T. Zinkevich, B. Reif and K. Saalwächter, *J. Magn. Reson.*, 2014, **248**, 8–12.
25 N. C. Nielsen, H. Bildsoe, H. J. Jakobsen and M. H. Levitt, *J. Chem. Phys.*, 1994, **101**, 1805–1812.
26 Z. Tosner, A. Purea, J. O. Struppe, S. Wegner, F. Engelke, S. J. Glaser and B. Reif, *J. Magn. Reson.*, 2017, **284**, 20–32.
27 H. Nagashima, J. Trebosc, O. Lafon, F. Pourpoint, P. Paluch, M. J. Potrzebowski and J.-P. Amoureux, *Sol. State Nucl. Magn. Reson.*, 2017, **87**, 137–142.
28 A. Wurl, K. Saalwächter and T. M. Ferreira, *Magn. Reson.*, 2023, **4**, 115–127.
29 H. M. McConnell, *J. Chem. Phys.*, 1958, **28**, 430–431.
30 A. G. Palmer, C. D. Kroenke and J. P. Loria, *Methods Enzymol.*, 2001, **339**, 204–238.
31 A. J. Baldwin and L. E. Kay, *J. Biomol. NMR*, 2013, **55**, 211–218.
32 P. Ma, J. D. Haller, J. Zajakala, P. Macek, A. C. Sivertsen, D. Willbold, J. Boisbouvier and P. Schanda, *Angew. Chem., Int. Ed.*, 2014, **53**, 4312–4317.
33 D. Marion, D. F. Gauto, I. Ayala, K. Giandoreggio-Barranco and P. Schanda, *ChemPhysChem*, 2019, **20**, 276–284.

34 M. D. Shannon, T. Theint, D. Mukhopadhyay, K. Surewicz, W. K. Surewicz, D. Marion, P. Schanda and C. P. Jaroniec, *ChemPhysChem*, 2019, **20**, 311–317.
35 K. Akasaka, S. Ganapathy, C. A. McDowell and A. Naito, *J. Chem. Phys.*, 1983, **78**, 3567–3572.
36 P. Tekely, D. Canet, J.-J. Delpuech and J. Virlet, *Magn. Res. Chem.*, 1990, **28**, S10–S14.
37 A. Krushelnitsky, T. Zinkevich, D. Reichert, V. Chevelkov and B. Reif, *J. Am. Chem. Soc.*, 2010, **132**, 11850–11853.
38 J. R. Lewandowski, H. J. Sass, S. Grzesiek, M. Blackledge and L. Emsley, *J. Am. Chem. Soc.*, 2011, **133**, 16762–16765.
39 A. Krushelnitsky and K. Saalwächter, *Magn. Reson.*, 2020, **1**, 247–259.

